

The Aharonov-Bohm Interference and Beating in Single-Walled Carbon Nanotube Interferometers

Jien Cao, Qian Wang, Marco Rolandi and Hongjie Dai*

*Department of Chemistry and Laboratory for Advanced Materials, Stanford University,
Stanford, CA 94305, USA*

Relatively low magnetic fields applied parallel to the axis of a chiral single-walled carbon nanotube are found causing large modulations to the p-channel or valence band conductance of the nanotube in the Fabry-Perot interference regime. Beating in the Aharonov-Bohm type of interference between two field-induced non-degenerate sub-bands of spiraling electrons is responsible for the observed modulation with a pseudo period much smaller than that needed to reach the flux quantum $\Phi_0 = h/e$ through the nanotube cross-section. We show that single-walled nanotubes represent the smallest cylinders exhibiting the Aharonov-Bohm effect with rich interference and beating phenomena arising from well-defined molecular orbitals reflective of the nanotube chirality.

* Email: hdai@stanford.edu

A hallmark of the Aharonov-Bohm (AB) effect [1] is conductance oscillations of metallic rings or cylinders as a function of enclosed magnetic flux with a period on the order of the flux quantum $\Phi_0 = h/e$ due to quantum interference [2,3]. Carbon nanotubes are chemically derived cylinders with atomically well-defined structures [4,5]. Multi-walled nanotubes (MWNT) have radius $r \sim 10$ nm and in magnetic fields parallel to the tube axis, conductance modulations with a period of $B_0 = \Phi_0 / \pi r^2 \sim 10$ T in magnetic field have been seen [6]. Single-walled nanotubes (SWNT) are ultra-small with $r \sim 1$ nm and the magnetic field needed to approach 1 Φ_0 flux through the nanotube cross section is $B_0 \sim 1000$ T, far beyond reach by experiments. We show here that in the Fabry-Perot interference [7] regime, beating in the AB-interference between two modes of spiraling electrons with non-degenerate wave-vectors causes conductance modulations under fields much smaller than that needed to reach 1 Φ_0 .

Ando and Ajiki suggested theoretically that the AB effect manifests in a SWNT by periodically modifying its band structure with a period of 1 Φ_0 in magnetic flux and ~ 1000 T in field [8]. A periodic change in the band-gap (\mathcal{E}_g) of the nanotube with $d\mathcal{E}_g/dB \sim 1$ meV/T was predicted. Optical adsorption experiments were able to confirm $d\mathcal{E}_g/dB \sim 1$ meV/T in semiconducting SWNTs in fields up to 45 T [9]. Recently, electrical measurements also detected similar changes in small band-gap SWNTs transport data inside the band-gap and Coulomb blockade near the band edge [10]. Much can still be done to probe the AB-effect in nanotubes for electronic states far away from the band-gaps and in the ballistic quantum interference regime [7,11] with conductance near $4e^2/h$.

Here, we report the AB effect manifested in the p-channel of a chiral small-gap SWNT in the Fabry-Perot interference regime. We clearly observe beating between two

non-degenerate modes of spiraling electrons along the nanotube ‘cylinder’ while circulating the circumference multiple-turns. Our analysis verifies the predicted band dispersion resulted from the AB effect. Also, by combining single-molecule raman spectroscopy and the AB-interference pattern from electron transport data, we can identify a (15,6) SWNT in the experimental sample.

Our devices comprised of suspended SWNTs grown by chemical vapor deposition (CVD) [12] across trenches (trench height $h \sim 300\text{nm}$) between pre-formed Pt contacts [13] (Fig. 1). The suspended tubes are free from substrate perturbations [13] and the high quality of the devices is responsible for the ‘clean’ experimental data in this work. Micro-raman spectroscopy [14] (Fig. 1c) performed on a $L = 815\text{ nm}$ long suspended tube (Fig. 1b) revealed three possible assignments to the tube $(m,n) = (14,8)$, (15,6) or (11,11) based on resonance conditions [14,15] with the 785 nm laser used. On the other hand, electrical data suggested a small band-gap nanotube [16,17] due to a gap (with $G \sim 0$) in the conductance vs. gate-voltage curve ($G-V_g$, Fig. 1d) recorded at $T=300\text{ mK}$. This narrowed down the nanotube to (14,8) or (15,6) with diameter $d \sim 1.5\text{ nm}$.

The p-channel conductance of the SWNT is high ($\bar{G} \sim 2.3e^2/h$) and exhibits an interference pattern in G vs. bias (V) and V_g , whereas the n-channel shows low conductance and Coulomb blockade (CB) (Fig. 1d). This difference is attributed to lower Schottky barrier to the p-channel of the nanotube than to the n-channel with Pt contacts [13,18]. For the p-channel, the conductance pattern is a result of Fabry-Perot like interference between two degenerate modes (sub-bands) of electrons in the nanotube ‘resonator’ confined by the two metal contacts [7].

When magnetic fields (-8T to 8T) were applied nearly parallel to the SWNT axis, we observed pronounced conductance modulations (Fig. 2) to the p-channel conductance despite the relatively low fields. The height of the conductance peaks (δG , relative to valleys) was reduced from $\sim 0.4e^2/h$ down to $\sim 0.08e^2/h$ as the field was varied from 0 to 8 T or to -8 T (Fig. 2b&2c). A slight shift in the positions of the conductance peaks along the V_g axis was also observed as the field increased to 8 T (Fig. 2b&2c).

In zero-field, the electron wave-vector $k = (k_\perp, k_\parallel)$ is quantized along the circumference as parallel lines (Fig. 3) such that the wave-function $\Psi(\mathbf{r} + \mathbf{R}_{mn}) = \Psi(\mathbf{r})$ where \mathbf{R}_{mn} is the wrapping vector of the nanotube. For a chiral (m, n) tube with $m \neq n$ and $m-n=3 \times \text{integer}$, two of the k_\parallel lines cross the inequivalent yet degenerate \mathbf{K}_1 and \mathbf{K}_2 points at the first Brillouin zone corners (Fig. 3a) and give rise to two degenerate sub-bands with zero band-gap. Perturbations such as curvature can cause the zero-gap states deviating from \mathbf{K}_1 and \mathbf{K}_2 by $\pm \Delta k_\perp^0$ respectively (Fig. 3a), resulting in a small band-gap for the two sub-bands (two opposite spiralling modes, Fig. 3c) at \mathbf{K}_1 and \mathbf{K}_2 but maintaining the degeneracy (Fig. 3b) with [8]

$$\varepsilon(k_\parallel) = \gamma \sqrt{(\Delta k_\perp^0)^2 + k_\parallel^2}, \quad (1)$$

where γ is the transfer integral and $2\gamma\Delta k_\perp^0 = \varepsilon_g^0$ is the band-gap.

In a magnetic field [8], the electron wave-function exhibits a phase shift by $\Psi(\mathbf{r} + \mathbf{R}_{mn}) = \Psi(\mathbf{r}) \exp(i\Phi / \Phi_0)$ due to the AB effect. This causes a uniform shift in the allowed states along k_\perp by $\Delta k_{AB} = \frac{2\pi}{|\mathbf{R}_{mn}|} \frac{\Phi}{\Phi_0}$ (Fig. 3d), i.e., shifting the k_\parallel lines for the \mathbf{K}_1 and \mathbf{K}_2 -related sub-bands closer to and further away from the zero-gap states (solid

circles in Fig.3a, 3d) respectively. This leads to increased and reduced band-gaps for the two sub-bands respectively and meanwhile lifts their degeneracy (Fig. 3e),

$$\varepsilon(k_{\parallel}) = \gamma \sqrt{\left(\Delta k_{\perp}^0 \pm \frac{2\pi}{|\mathbf{R}_{mn}|} \frac{\Phi}{\Phi_0} \right)^2 + k_{\parallel}^2} \quad ('+' \text{ for } \mathbf{K}_1, '-' \text{ for } \mathbf{K}_2 \text{ sub-band}) \quad (2)$$

The change of bandgap is $d\varepsilon_g / dB \sim \pm \gamma \frac{2\pi}{|\mathbf{R}_{mn}|} \frac{d\Phi / dB}{\Phi_0} \sim \pm 1 \text{ meV/T}$. Due to the

lifted degeneracy between the \mathbf{K}_1 and \mathbf{K}_2 related sub-bands by the magnetic field, at a given Fermi energy ε in the p-channel, two different wave-vector amplitudes now exist (Fig.3e&3f), i.e.,

$$|k_{1,2}| = \sqrt{\varepsilon^2 - \left(\Delta k_{\perp}^0 \pm \frac{2\pi}{|\mathbf{R}_{mn}|} \frac{\Phi}{\Phi_0} \right)^2} \quad ('+' \text{ for } \mathbf{K}_1, '-' \text{ for } \mathbf{K}_2 \text{ sub-band}) \quad (3)$$

for the two modes of electrons with opposite orbiting directions around the nanotube.

We calculated G vs. B and V_g for SWNTs based on interference between non-degenerate $\pm k_1$ and $\pm k_2$ modes (Fig. 4) in a way similar to the Fabry-Perot interference for degenerate modes using the multi-channel Landau-Buttiker formalism and S-matrices [7,19]. Conversion of ε to V_g was based on matching experimental G . vs. V and V_g under $B=0$ (Fig. 1d lower inset) with calculated G . vs V and ε (data not shown). The band-gap of the SWNT ε_g^0 is calculated from (m,n) indices based on the curvature induced band-gap model [17]. Numerically calculated G vs. B and V_g for the (15, 6) SWNT give excellent agreement with experimental data (Fig. 2b&2c vs. 4a) in terms of the conductance peaks height modulation vs. B and the amount of peak position shift along V_g under increased field. Calculations based on the (14,8) SWNT do not agree with

experiment with much smaller G vs. B modulations than experimental data (Fig.4b vs. Fig.2b&2c).

Up to high fields, simulations reveal that the conductance of the (15,6) SWNT is modulated by B with a pseudo-period of $B_0' \sim 20\text{-}30$ T (dependent on V_g or ϵ) and the conductance peak-shift along V_g becomes more apparent and show ‘arching’ (Fig. 4a right panel). The experimentally observed δG vs. B and V_g well corresponds to such evolutions, albeit in a smaller range of B field. The physics underlying the G modulation with $B_0' \ll B_0$ is beating between two non-degenerate modes of spiraling electrons.

One sees that in a SWNT with greater $|\Delta k_\perp^0|$ or larger chiral angle (defined as $\theta=0$ for armchair and 30° for zig-zag tubes), the difference in the number of turns of circumference-orbiting between the two modes when traversing the tube length L is greater than in a tube with zero or small chiral angle. For various $m-n=3 \times \text{integer}$ SWNTs with similar diameters, beating modulation is the most rapid in zig-zag tubes, followed by chiral tubes and is non-existent in arm-chair SWNTs (Fig. 4c), as confirmed by simulations. By setting the field-induced phase shifts between the two modes over a length of L to 2π , we find an approximate form of B_0' ,

$$B_0'(\epsilon) \approx \frac{\pi}{L} \frac{r}{\epsilon_g^0} \frac{2\epsilon}{B_0} \propto \frac{\pi}{L} \frac{r}{\sin(3\theta)} \cdot B_0 \quad (4)$$

suggesting that the beating modulation period is reduced from B_0 (corresponding to $1 \Phi_0$) by a factor of $r/L \sim 10^{-3}$ and is highly sensitive to the tube chiral angle θ through the $1/\sin(3\theta)$ relation. Note that $\theta=14^\circ$ and 9° for (15,6) and (14,8) SWNT respectively, and the difference in chiral angles leads to a large discernable difference in B_0' according to Eq. (4) and simulations (Fig. 4a vs. 4b right panels). For an armchair nanotube, no sub-

band splitting occurs due to symmetry and thus no beating-like conductance modulation ($\theta=0, B_0' \sim \infty$) by axial magnetic fields (Fig. 4c). Nevertheless, a band-gap is opened for the two degenerate sub-bands and the band-gap change and resulting non-linearity in $\varepsilon(k)$ lead to shifting (or ‘arching’) (Fig. 4c right panel) of the conductance peaks along V_g under increasing B . This is the regular AB effect (in the absence of beating) with a $1 \Phi_0$ period in magnetic flux and is universal for nanotubes of all chirality (Fig. 4a,b and c right panels).

The observation of quantum beats for the Aharonov-Bohm effect is to our knowledge unprecedented in mesoscopic systems and is a result of well-defined molecular orbitals of nanotubes in magnetic fields. Large band-gap semiconductor SWNTs with low Schottky-barrier p-channels in the Fabry-Perot regime [18] could exhibit much more rapid beats than the small band-gap SWNTs. Clearly, many future opportunities exist for elucidating quantum interference and beating between well-defined molecular orbitals.

We thank Ali Javey for discussions. This work is supported by the MARCO MSD Focus Center, SRC/AMD, INMP, a Packard Fellowship and a Dreyfus Teacher-Scholar.

Figure Captions:

Figure 1. A suspended chiral-nanotube quantum wire. (a) Schematic device structure.

Nanotubes were synthesized across Pt electrodes over trenches at 800-820°C to produce SWNTs with diameters $d < 2$ nm. (b) Electron micrographs of the device layout (left image) and actual suspended nanotube (right image, $L \sim 815$ nm) used for this work. (c) A resonance micro-Raman spectrum (Renishaw, laser $\lambda=785$ nm, spot size $1\mu\text{m}$ scanned over the trench) showing the radial breathing mode (RBM) of a $d \sim 1.5$ nm SWNT with possible chirality assignments of (11,11), (14,8) and (15,6) based on the RBM shift at $\omega=163 \pm 4\text{cm}^{-1}$. (d) $G-V_g$ characteristics recorded at $T=300\text{mK}$ in a ^3He cryostat under bias $V=1\text{mV}$. Left inset: G (represented by color, dark blue: $\sim 2e^2/h$, bright white: $\sim 2.4 e^2/h$) vs. bias V and V_g for the p-channel showing Fabry-Perot interference pattern. Right inset: G vs. V and V_g for the n-channel displaying Coulomb blockade diamonds.

Figure 2. Experimental data of a nanotube interferometer in magnetic fields. (a) $G-V_g$ characteristics for the suspended SWNT in magnetic fields (angle to tube axis $\sim 9^\circ$) from 0 to 8 T recorded at $T=300$ mK under $V=1\text{mV}$. The conductance peaks monotonically decrease from 0 to 8 T. (b) A zoom-in view of (a). From top to bottom curves, $G-V_g$ characteristics in field $B=0$ to 8T, in 2 T steps. Notice slight shifts in the peak positions to the left at higher fields. (c) A plot of G (represented by color) vs. V_g and magnetic field B (-8 T to 8T) based on 160 $G-V_g$ curves from $B = -8\text{T}$ to 8T in 0.1 T steps. Color scale bar unit: e^2/h . The slight shifts of conductance peaks positions in (b) are reflected in the slight arching of the interference stripes as highlighted by the dashed line.

Figure 3. The AB effect in a multi-mode nanotube interferometer. (a) The first Brillouin zone of a small-gap chiral SWNT (in zero magnetic field). Only two parallel lines (dashed) of the allowed states closest to the zero band-gap points (the two solid circles near the inequivalent \mathbf{K}_1 and \mathbf{K}_2 corner points respectively) are shown. Perturbations cause the zero band-gap states deviating from \mathbf{K}_1 and \mathbf{K}_2 by $\pm \Delta k_{\perp}^0$ due to symmetry and the opening of a small-gap along the two dashed lines (\mathbf{K}_1 and \mathbf{K}_2 sub-bands). (b) Dispersion $\varepsilon(k)$ relations for the two degenerate sub-bands near \mathbf{K}_1 (blue curve) and \mathbf{K}_2 (red curve) respectively. $k_{\parallel}=0$ is defined for the states where the conduction and valence band are the closest. (c) Two degenerate modes of spiraling electrons in zero-field. (d) In a magnetic field parallel to the tube axis, the electronic states (dashed lines) shift by Δk_{AB} due to the AB effect, leading to lifting of the degeneracy between the two sub-bands. (e) Dispersion curves for the two non-degenerate sub-bands in a magnetic field of $B=8\text{T}$. (f) Two non-degenerate modes of spiraling electrons in a magnetic field.

Figure 4. Simulation of Aharonov-Bohm interference and beating versus nanotube chirality. (a), (b) and (c) are simulation results for (15,6), (14,8) and (11,11) SWNT respectively. Left panel: Calculated G - V_g curves in fields of $B=0$ to 8T from top to bottom in 2T steps. Middle panel: Calculated 2-D plot of G vs. V_g and B in a small field range -8T to 8T. Right panel: Calculated 2-D plot of G vs. V_g and B over a wider field range of -30T to 30 T showing that shifting or arching of the conductance peaks is universal for the three different chirality nanotubes. Our simulations here used precise $\varepsilon(k)$ dispersions such as Eq. 2 and 3 instead of linear approximations. Note that we have

also considered and excluded the possibility of a (16,4) tube in the experimental sample.

The (16,4) tube has a chiral angle of 19° , larger than the three tubes considered in this figure and exhibit more rapid beating period than the experimental data. Further, the (16,4) tube has $d \approx 1.43$ nm, outside of the range of $d=1.45$ - 1.53 nm determined from the Raman resonance condition¹⁵ of d (in nm) $= 223.5/(\bar{\omega}-12.5)$ for $\bar{\omega}=163 \pm 4\text{cm}^{-1}$ (Fig. 1c).

References and Notes

- [1] Y. Aharonov and D. Bohm, Phys. Rev. 115, 485 (1959).
- [2] R. A. Webb, S. Washburn, C. P. Umbach, *et al.*, Phys. Rev. Lett. 54, 2696 (1985).
- [3] V. Chandrasekhar, M. J. Rooks, S. Wind, *et al.*, Phys. Rev. Lett. 55, 1610 (1985).
- [4] M. S. Dresselhaus, G. Dresselhaus, and P. Avouris, in *Topics in Appl. Phys.* (Springer, Berlin, 2001), Vol. 80.
- [5] H. Dai, Surf. Sci. 500, 218 (2002).
- [6] A. Bachtold, C. Strunk, J. P. Salvetat, *et al.*, Nature 397, 673 (1999).
- [7] W. Liang, M. Bockrath, D. Bozovic, *et al.*, Nature 411, 665 (2001).
- [8] H. Ajiki and T. Ando, J. Phys. Soc. Jpn. 62, 1255 (1993).
- [9] J. Kono, G.N. Ostojic, S. Zaric, *et al.*, Appl. Phys. A 78, 1093 (2004).
- [10] E. D. Minot, Y. Yaish, V. Sazonova, *et al.*, Nature 428, 536 (2004).
- [11] J. Kong, E. Yenilmez, T. W. Tombler, *et al.*, Phys. Rev. Lett. 87, 106801 (2001).
- [12] J. Kong, H. Soh, A. Cassell, *et al.*, Nature 395, 878 (1998).
- [13] J. Cao, Q. Wang, D. Wang, *et al.*, cond-mat/0312239.
- [14] A. Jorio, R. R Saito, J. H. Hafner, *et al.*, Phys. Rev. Lett. 86, 1118 (2001).
- [15] S. M. Bachilo, M. S. Strano, C. Kittrell, *et al.*, Science 298, 2361 (2002).
- [16] C. Zhou, J. Kong, and H. Dai, Phys. Rev. Lett. 84, 5604 (2000).
- [17] A. Kleiner and S. Eggert, Phys. Rev. B 63, 073408 (2001).
- [18] A. Javey, J. Guo, Q. Wang, *et al.*, Nature 424, 654 (2003).
- [19] M. Buttiker, Y. Imry, R. Landauer, *et al.*, Phys Rev B 31, 6207 (1985).

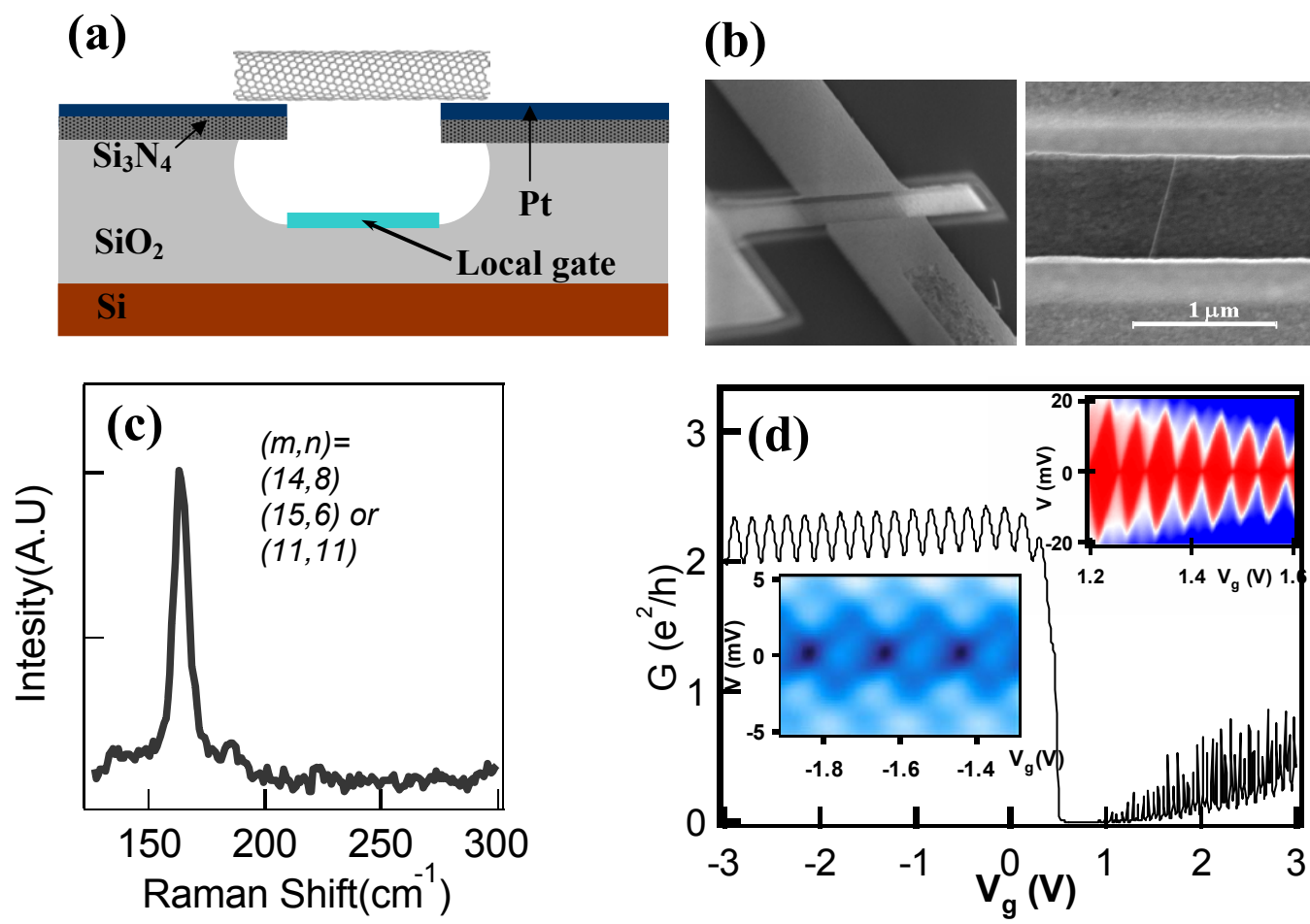


Fig. 1

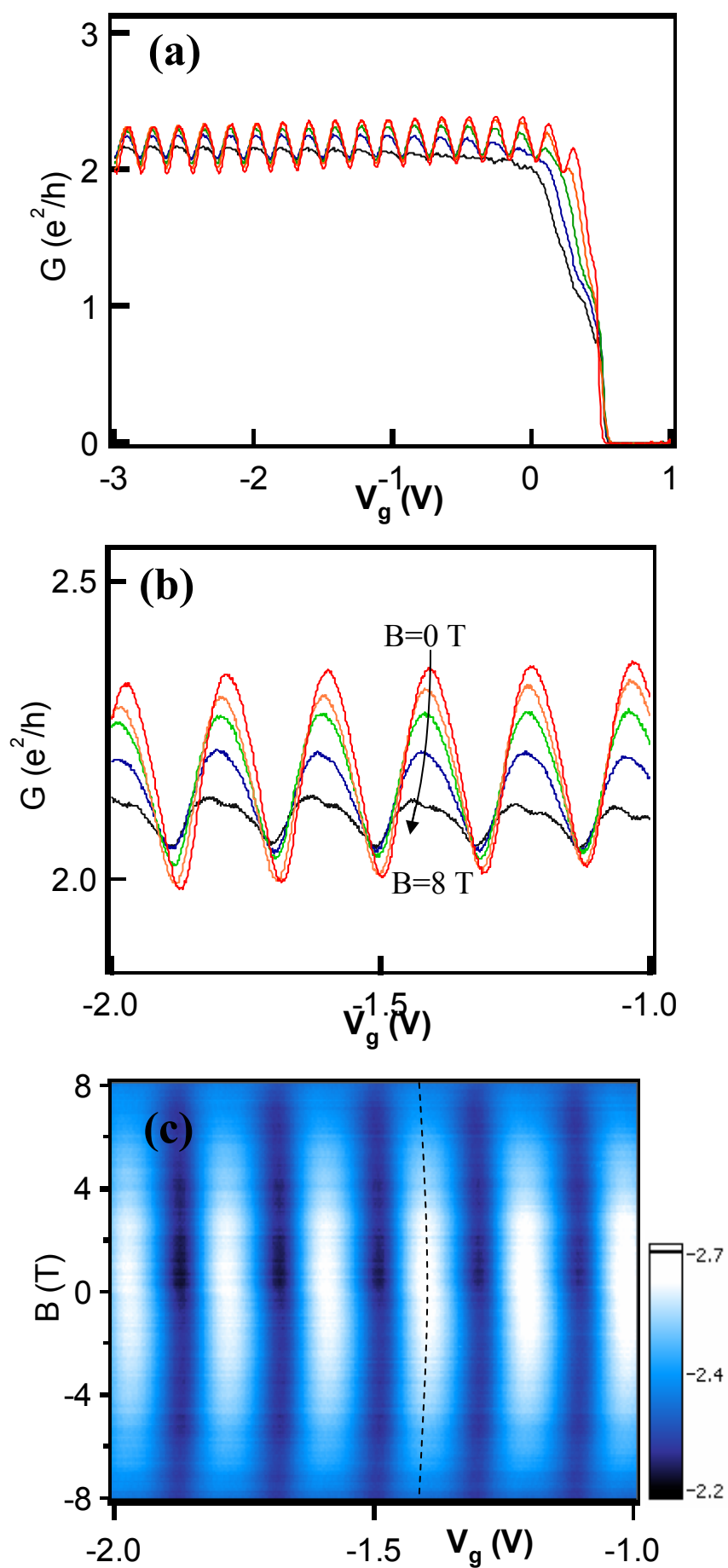


Fig. 2

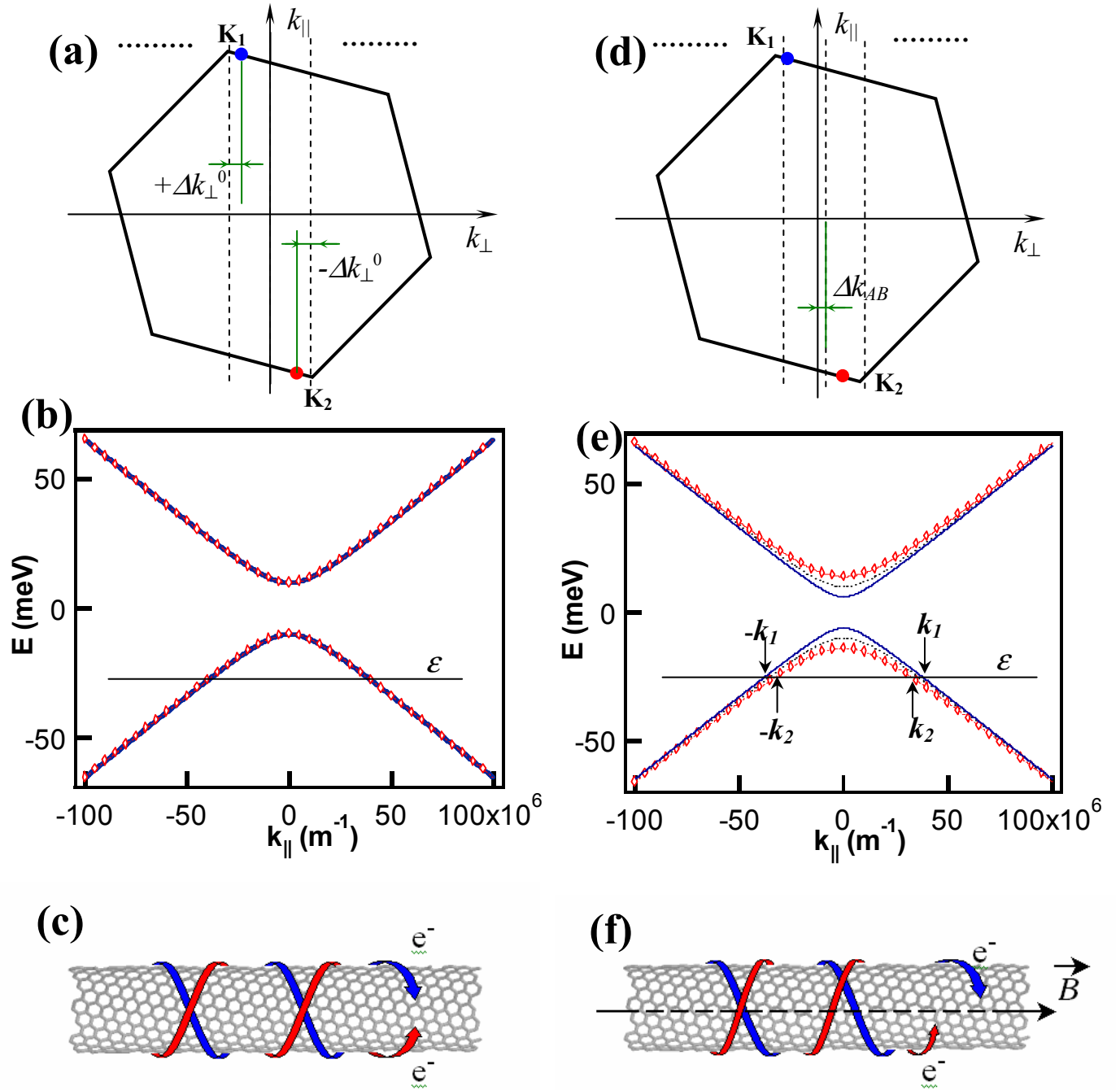


Fig. 3

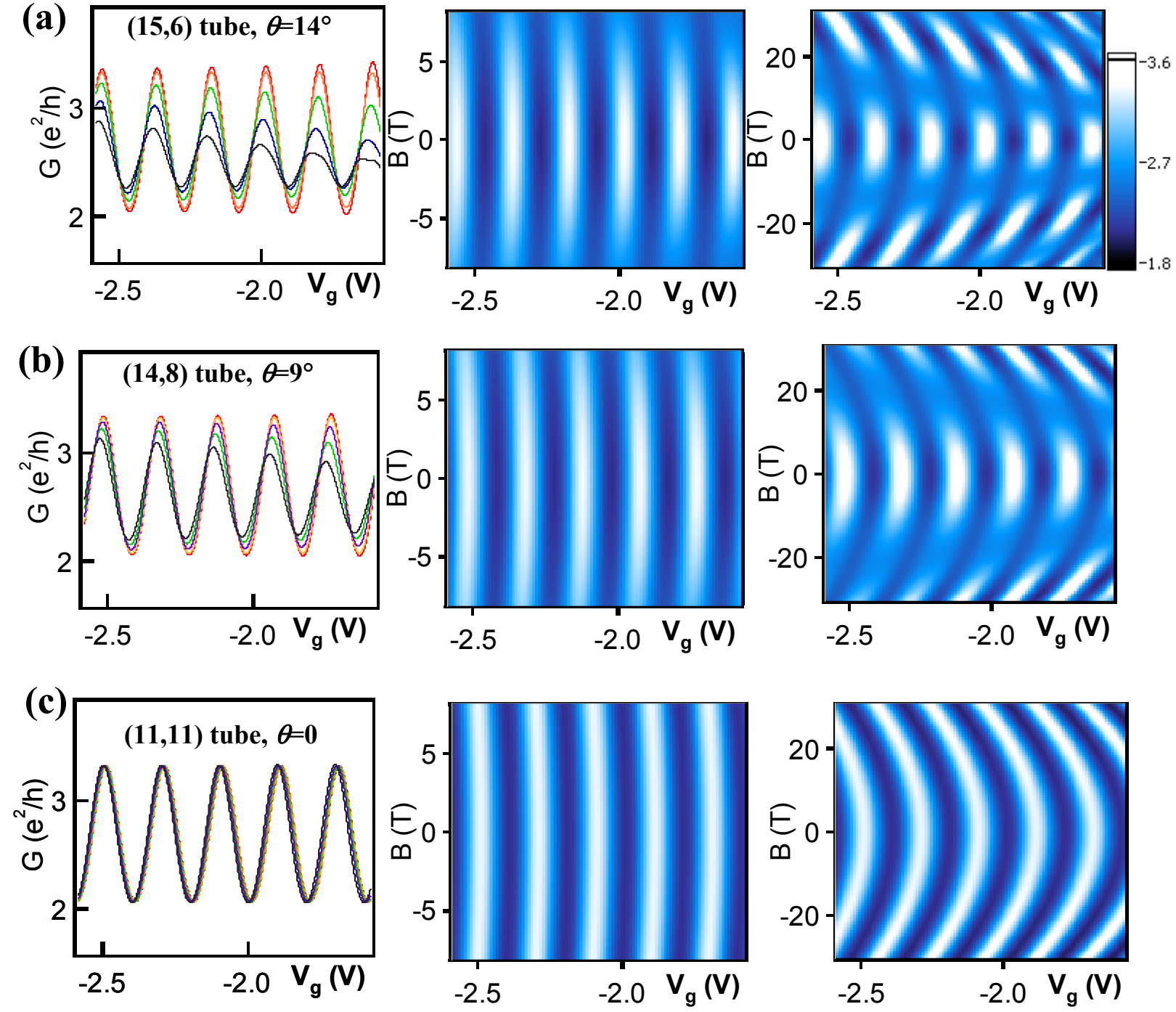


Fig. 4